Geophysical Journal International

Geophys. J. Int. (2020) **221,** 893–904
doi: 10.1093/gji/ggaa041
Advance Access publication 2020 January 24
GJI General Geophysical Methods

A new method to estimate ocean-bottom-seismometer orientation using teleseismic receiver functions

Hong Zheng ,[1,2,3] Jianke Fan ,[1,2,5] Dapeng Zhao,[4] Cuilin Li,[1,2,5] Dongdong Dong,[1,2,5] Guangxu Zhang[1,5] and Xiujuan Wang[1,5]

[1] *CAS Key Laboratory of Marine Geology and Environment, Institute of Oceanology, Chinese Academy of Sciences, Qingdao* 266071*, China. E-mail: fanjianke@qdio.ac.cn*
[2] *Laboratory for Marine Geology, Qingdao National Laboratory for Marine Science and Technology, Qingdao* 266061*, China*
[3] *University of Chinese Academy of Sciences, Beijing* 100049*, China*
[4] *Department of Geophysics, Graduate School of Science, Tohoku University, Sendai* 980–8578*, Japan*
[5] *Center for Ocean Mega-Science, Chinese Academy of Sciences, Qingdao, China*

Accepted 2020 January 14. Received 2019 January 7; in original form 2019 May 13

SUMMARY

The orientation of an ocean-bottom-seismometer (OBS) is a critical parameter for analysing three-component seismograms, but it is difficult to estimate because of the uncontrollable OBS posture after its deployment. In this study, we develop a new and effective method to estimate the OBS orientation by fitting the amplitude of direct *P* wave of teleseismic receiver functions. The reliability of this method is verified using synthetic data and observed waveforms recorded at land seismic stations in Shandong Province, China. Our extensive synthetic tests show that our new method is little affected by a thin sedimentary layer that has a low *S*-wave velocity. The orientations of OBS stations that we deployed in the Yap subduction zone in the Western Pacific Ocean are estimated and corrected using our new method. After the correction, the direct *P* waves of teleseismic receiver functions show very good consistency. The effects of white and coloured noise in different levels, epicentral distance and backazimuth are also investigated, and the results show that these factors have small effects on the new method. We also examine the effect of sensor tilting on estimation of the OBS orientation, and find that a tilting correction should be made before the misorientation correction. We compare the OBS orientations determined with the new method and other methods and find that they are generally consistent with each other. We also discuss advantages and shortcomings of various methods, and think that our new method is more robust than the existing methods.

Key words: Time-series analysis; Body waves; Computational seismology; Seismic instruments.

1 INTRODUCTION

Accurate orientation of three-component broad-band seismometers is essential in almost all seismological studies, such as analysis of receiver functions (RFs) and shear wave splitting measurements. Estimating the orientation of a seismic sensor is then crucial in seismic data processing, which has been proved to have a great influence on seismological studies, such as the off-great-circle propagation of long-period surface waves (Laske 1995), anisotropic structure of the upper mantle using the SKS splitting method (Long *et al.* 2009), and comparison of observed and synthetic records (Rueda & Mezcua 2015). Zahradnik & Custodio (2012) found that 10° and 30° deviations of the sensor orientation could result in amplitude errors of original waveform on the order of 10–40 per cent and 30–90 per cent, respectively, which could further cause wrong estimation of seismic parameters, such as the dip angle of a crustal layer, and anisotropic parameters of the crust and upper mantle (Wang *et al.* 2016).

For land seismic stations, the sensor orientation is generally corrected by determining the direction of the magnetic North Pole based on compass, and the global magnetic declination is utilized to calibrate the direction of the geographic North Pole (Ringler *et al.* 2013). Recently, a new and more accurate method is adopted for the installation of land seismic stations, which uses the fiber-optic gyrocompass and sunshot (such as theodolite or Global Positioning System) to find the true north and to transfer the reference line, respectively (Wang *et al.* 2016).

However, the above-mentioned methods are usually inapplicable for the misorientation correction of ocean-bottom-seismometers (OBSs), because the OBSs fall down freely during deployment and

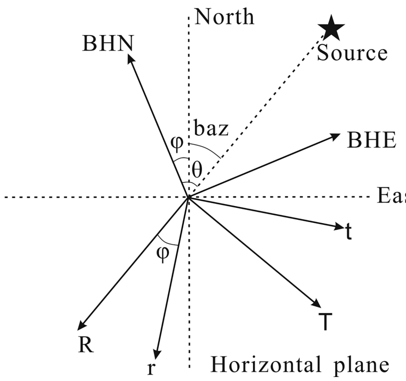

Figure 1. A schematic diagram showing the relationship between a sensor misorientation (φ), observed backazimuth (θ) and the backazimuth after correction (baz). The star denotes a seismic event. BHN and BHE denote northern and eastern components of the OBS sensor before correction. r and t represent the radial and transverse components with the sensor misorientation (φ), whereas R and T represent the radial and transverse components without misorientation.

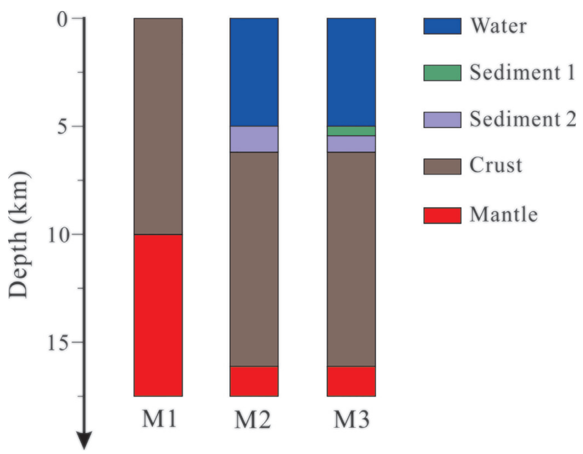

Figure 2. Three velocity models adopted for the synthetic tests. The model parameters are listed in Table 1.

Table 1. Physical parameters of the three velocity models as shown in Fig. 2. ρ is density, V_P and V_S are P- and S-wave velocities, respectively. The mantle is defined as a half-space below the crust.

Layer	ρ (g cm^{-3})	V_P (km s^{-1})	V_S (km s^{-1})	Thickness (km)		
				M1	M2	M3
Water	1.03	1.50	0	0	5.0	5.0
Sediment 1	1.70	1.60	0.16	0	0	0.1
Sediment 2	2.00	2.10	0.70	0	0.3	0.2
Crust	2.70	6.10	3.55	10.0	10.0	10.0
Mantle	4.40	8.10	4.55	∞	∞	∞

cannot be manipulated artificially. Since 1980s, many solutions have been proposed for this problem, such as the Rayleigh or Love wave polarization method (e.g. Laske *et al.* 1994; Laske 1995; Baker & Stevens 2004; Stachnik *et al.* 2012; Rueda & Mezcua 2015), the P-wave particle motion method (Niu & Li 2011; Wang *et al.* 2016), the ambient-noise correlation method (Zha *et al.* 2013), and the tangential receiver-function method (Janiszewski & Abers 2015). These methods are all based on a traverse scanning strategy with a small interval (e.g. 1°) to determine the optimal azimuth after 360°

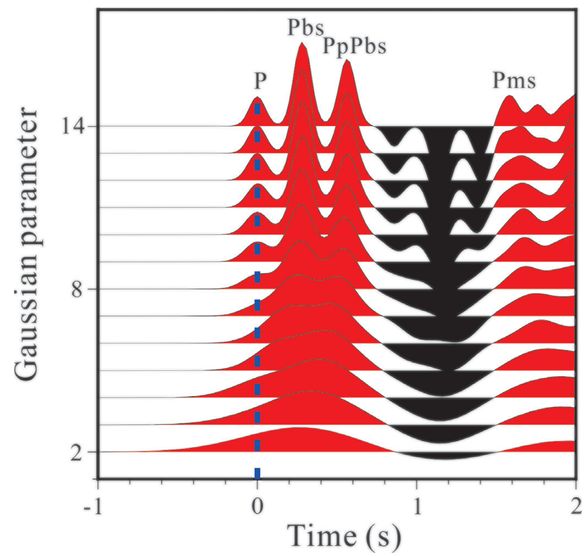

Figure 3. RFs generated for the model M2 with different Gaussian parameters. The blue dashed line denotes the position of time 0 s. Pbs denotes a converted phase at the boundary between the sedimentary layer and the basement, and Pms denotes a converted phase at the Moho discontinuity. PpPbs denotes a reverberation in the sedimentary layer. Ray paths of these seismic phases are shown in Fig. S1(c).

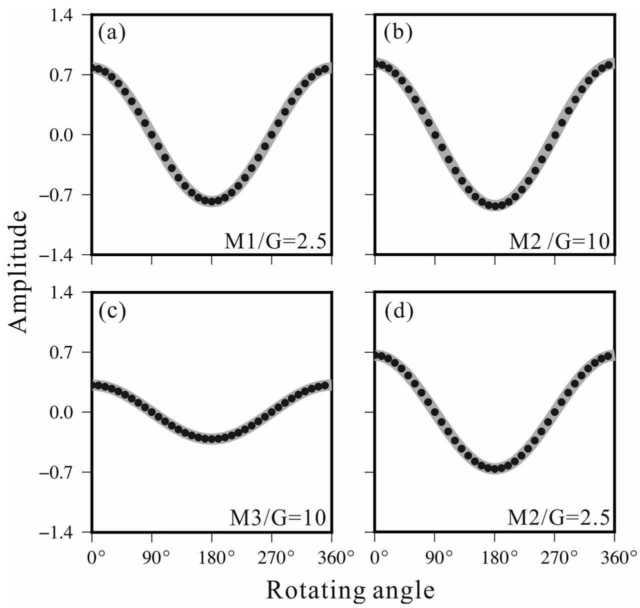

Figure 4. Variations of the amplitude with different rotating angles (dots) for different models and Gaussian parameters (G) when the misorientation is 0°. The thick grey lines are the fitting cosine curves. The fitting formulas are (a) : $A_{rf}(x) = 0.7802 * \cos(x + 1.109 \times 10^{-7})$, (b) : $A_{rf}(x) = 0.8301 * \cos(x + 4.075 \times 10^{-8})$, (c) : $A_{rf}(x) = 0.3152 * \cos(x + 1.417 \times 10^{-8})$ and (d): $A_{rf}(x) = 0.6638 * \cos(x + 1.372 \times 10^{-8})$.

rotation. However, these methods may not be very effective because of high noise level near seafloor. A method proposed by Lim *et al.* (2018) on the basis of harmonic decomposition is less dependent on the ambient noise and can obtain more stable and reliable results. However, this method needs a larger back-azimuth coverage, which is very difficult to achieve for most OBS arrays.

During our analysis of teleseismic radial receiver functions, we find that the polarity and amplitude of direct P wave are significantly

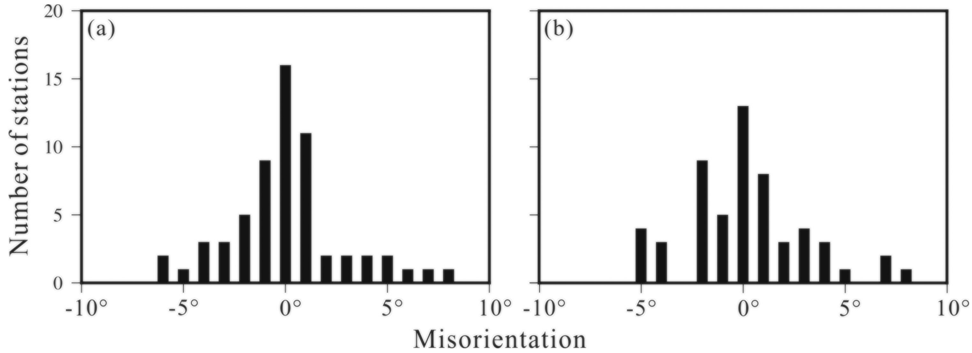

Figure 5. Histograms for the number of land seismic stations with different misorientations estimated with our new method (a) and the tangential receiver-function method (b). The misorientation interval is 1°.

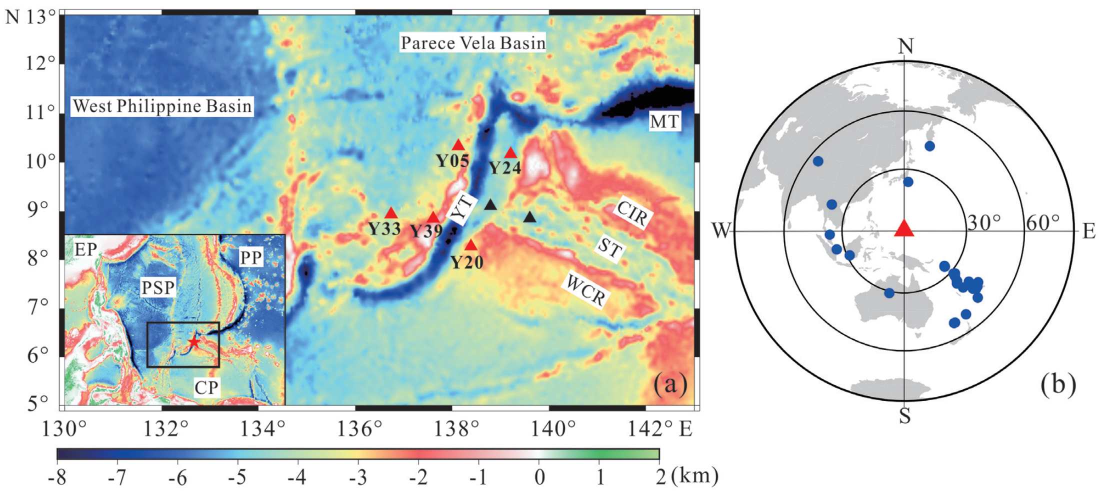

Figure 6. Distribution of (a) OBS stations (triangles) and (b) teleseismic events (blue dots) used to estimate the OBS misorientation. The red and black triangles in (a) denote the OBSs with valid and invalid data, respectively. The black box and red star in the inset map in (a) show the location of this study area and the Yap Trench (YT). EP, the Eurasian Plate; PP, the Pacific Plate; PSP, the Philippine Sea Plate; CP, the Caroline Plate; MT, the Mariana Trench; CIR, the Caroline Island Ridge; ST, the Sorol Trough; WCR, the West Caroline Ridge.

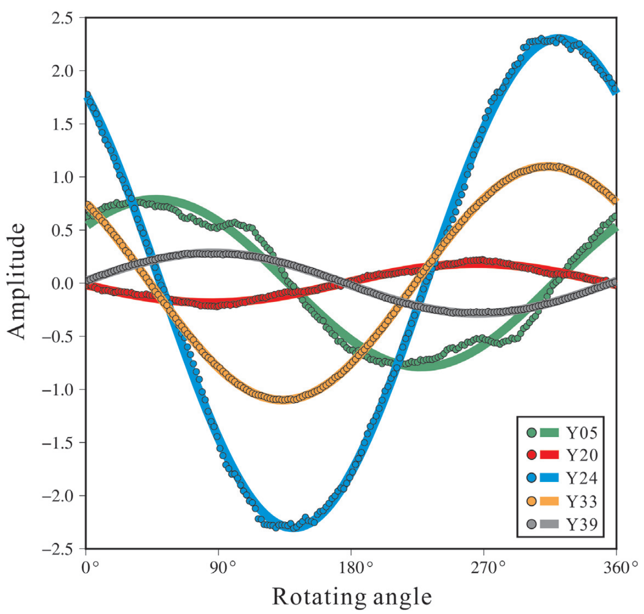

Figure 7. Amplitudes of direct *P* waves of stacked receiver functions (colour dots) and the fitting cosine curves (colour lines) for the five OBS stations deployed in the Yap region.

correlated with the OBS orientation as a cosine function. On the basis of this observation, here we propose a new and effective method to determine the OBS orientation accurately by fitting the amplitude of direct *P* wave of RFs (APRF) using a cosine function. We think that this APRF method will be very useful for the OBS data processing and related seismological studies from now.

2 METHOD

Teleseismic receiver function is a time-series showing the relative response of the Earth structure beneath a seismic station, which has become a conventional tool of seismic data analysis to study the local crustal and upper mantle structure (e.g. Vinnik 1977; Langston 1979; Owens *et al.* 1984; Ammon *et al*. 1990; Julià *et al.* 2000; Zhu & Kanamori 2000). To obtain a reasonable RF, the amplitude of direct *P* wave of all seismic events should be the maximum at time 0 s in the radial–transverse–vertical (*R*–*T*–*Z*) coordinate system. However, if a sensor is mis-oriented, the amplitude of direct *P* wave of RFs would be smaller. Furthermore, the polarity of the direct *P* wave would be converted. Therefore, in this study we first show the relationship between the maximum amplitude of direct *P* wave of the RFs and the sensor misorientation.

Assuming that the OBS misorientation is φ that is the angle between BHN and the geographical north as shown in Fig. 1. If

Table 2. Fitting formulas, OBS misorientations, *R*-squares and numbers of RFs used to estimate the OBS misorientations.

Station	Fitting formula	Misorientation	*R*-square	Number of RFs
Y05	$A_{rf}(x) = 0.789 * \cos(x - 47.43)$	$-47.43° \pm 6.45°$	0.9769	19
Y20	$A_{rf}(x) = 0.183 * \cos(x + 95.07)$	$95.07° \pm 2.26°$	0.9789	13
Y24	$A_{rf}(x) = 2.303 * \cos(x + 39.24)$	$39.24° \pm 4.23°$	0.9989	21
Y33	$A_{rf}(x) = 1.100 * \cos(x + 46.46)$	$46.46° \pm 4.24°$	1.000	8
Y39	$A_{rf}(x) = 0.285 * \cos(x - 85.88)$	$-85.88° \pm 5.62°$	0.9993	18

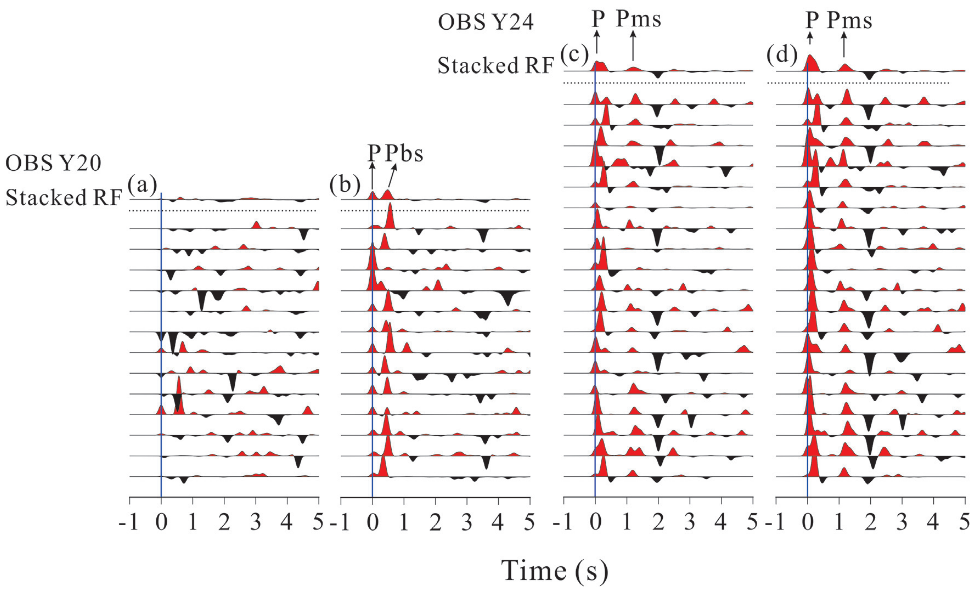

Figure 8. Receiver functions before (a, c) and after (b, d) the misorientation correction for the OBS stations Y20 (a, b) and Y24 (c, d). The stacked receiver functions are shown at the top. The Gaussian parameter is 10.

there is no misorientation, the two horizontal components of OBS will be rotated to radial (*R*) and transverse (*T*) directions according to the backazimuth along the great-circle path. However, when the OBS misorientation is φ, the two horizontal components will be rotated to *r* and *t* directions, respectively. The angle between *r* and *R* is also φ (Fig. 1). Then we have:

$$A_r = A_R * \cos\varphi + A_T * \sin\varphi, \tag{1}$$

where A_r, A_R and A_T represent the amplitudes of direct *P* wave in the *r*, *R* and *T* directions, respectively. Theoretically, A_T is zero, then eq. (1) becomes:

$$A_r = A_R * \cos\varphi. \tag{2}$$

Similarly, the amplitude of direct *P* wave of RF after deconvolution should be also consistent with eq. (2):

$$A_{rf} = A_{Rf} * \cos\varphi, \tag{3}$$

where A_{rf} and A_{Rf} denote the amplitudes of direct *P* wave of RF after deconvolution calculated in *r* and *R* components, respectively. Then eq. (3) can be rewritten as a fitting formula as follows:

$$A_{rf}(x) = C_f * \cos(x + \varphi), \tag{4}$$

where $A_{rf}(x)$ denotes the amplitude of direct *P* wave of RF with the sensor misorientation φ after rotating *x* degrees, and C_f is a coefficient.

The sensor misorientation can be obtained by fitting eq. (4). First, seismic events with relatively high signal-to-noise ratio (SNR) are selected, which depends on the data quality. In this study, the SNR in synthetic tests is defined as the ratio of energy within 0.5 s after the direct *P*-wave arrival time calculated for the iasp91 model (Kennett & Engdahl 1991) to that before the direct *P*-wave arrival time, whereas the SNR for the OBSs is the ratio of energy within 10 s after the manually picked direct *P*-wave arrival time to that before the direct *P*-wave arrival time. The seismic events recorded at our OBSs that have SNR > 4 are selected. Next, the two horizontal components are rotated from 1° to 360° with an interval of 1° to obtain 360 temporary horizontal components, and then they are converted to the *R–T–Z* coordinate system according to the backazimuth (Fig. 1). After that, the amplitudes at time 0 s of RFs are calculated to get a total of 360 values as measured data. Finally, eq. (4) is used to fit these 360 values to obtain φ by using a least-squares method, which is considered as the sensor misorientation.

3 SYNTHETIC TESTS

A number of synthetic tests are performed to confirm the effectiveness of our new method. Three theoretical models are constructed, two of which include water and sedimentary layers (Fig. 2 and Table 1). The thicknesses, velocities and densities of the water and sedimentary layers are derived from a previous work (Zhang *et al.* 2019) and the Deep Sea Drilling Project (DSDP, Pimm *et al.* 1971) in and around the Yap subduction zone in the Western Pacific Ocean. Then three-component synthetic waveforms are calculated using the wavenumber integration method (Herrmann & Mandal 1986) with a reference ray parameter of 0.07 s km^{-1} for the three models

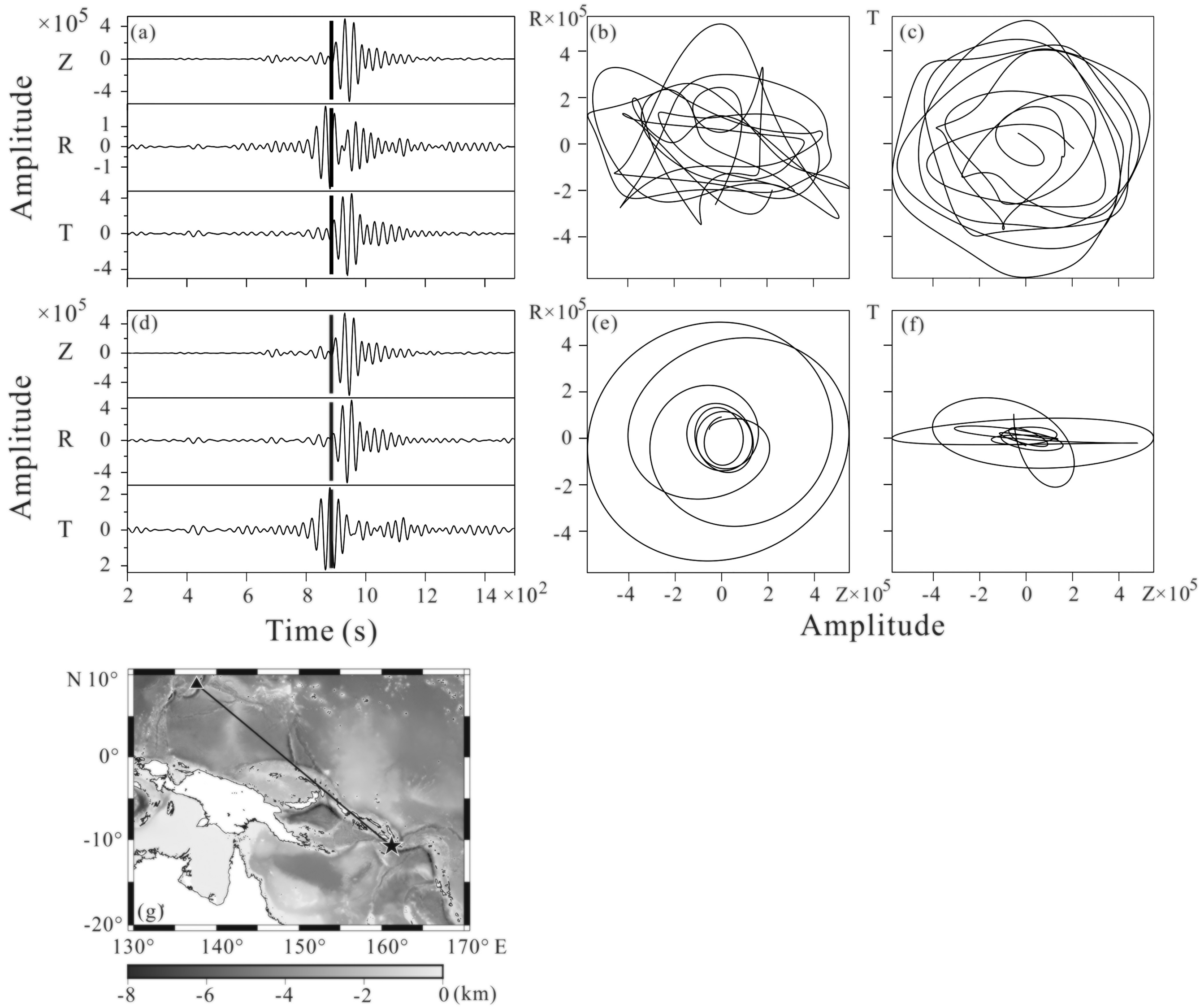

Figure 9. Three-component seismograms (a, d) and particle motions on the *Z*–*R* plane (b, e) and *Z*–*T* plane (c, f) in 200 s after the estimated Rayleigh-wave arrival time [vertical thick lines in (a, d)] of an earthquake (M_w 7.8) recorded at the OBS station Y39 with bandpass filtering (0.02–0.04 Hz) before (a, b, c) and after (d, e, f) the misorientation correction. (g) A map showing locations of the OBS station Y39 (triangle) and the earthquake (star) whose epicentral distance and focal depth are 30.55° and 40 km, respectively.

M1–M3, and the RFs are calculated after the ITER-deconvolution (Kikuchi & Kanamori 1982; Ligorria & Ammon 1999).

In RFs, a phase lag of direct *P* wave would occur due to a thin and/or low V_S sedimentary layer (Fig. S1), which causes inaccurate RF results (Sheehan *et al.* 1995; Audet 2016; Kawakatsu & Abe 2016). However, in our analysis, the direct *P* wave is not lagged but is covered by a converted phase Pbs at the boundary between the sedimentary layer and the basement due to a lower Gaussian parameter and a higher amplitude of Pbs wave when there is a larger impedance contrast at the boundary. When the Gaussian parameter increases, the direct *P* wave is gradually separated from the Pbs wave (Fig. 3). Therefore, our method would be effective for a higher Gaussian parameter when evaluating the OBS misorientation, to separate the direct *P* wave and avoid the effect of thin and/or low V_S sedimentary layers as much as possible. However, a lower Gaussian parameter (e.g. 2.5) is feasible when assessing the misorientation of a land station, because the effect of sedimentary layers (if any) beneath land stations is not very serious.

For the synthetic tests, three-component synthetic waveforms for the three models are firstly obtained by forward-modelling with a backazimuth of 0°. Obviously, the misorientations of these synthetic data are all 0°. To know how the amplitude of direct *P* wave of RFs changes with different rotating angles, the synthetic seismograms are rotated from 0° to 360° with an interval of 10°, and then 36 radial RFs for each model are obtained after the ITER-deconvolution is performed with the Gaussian parameters of 2.5 and 10, respectively (Fig. S2). For different models, similar features show up, that is the amplitude of RFs changes with different rotating angles, and the polarity is even reversed when the rotating angle is between 90° and 270° (Figs S2a–S2c). Then the 36 amplitudes with different rotating angles for each model are fitted as observed data, and the fitting curves are shown in Figs 4(a)–(c). The estimated misorientations by our method for models M1, M2 and M3 are all about 0°. In addition, we determine the fitting results with fixed misorientations of 135° and 225° (Fig. S3), whose errors are almost 0°.

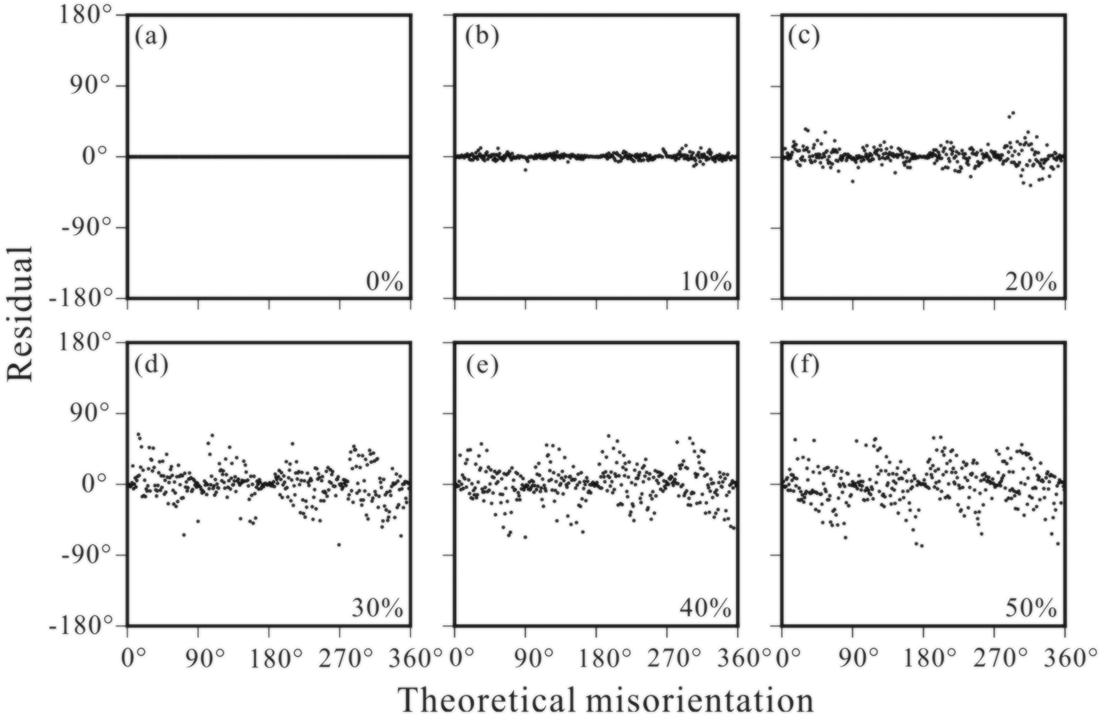

Figure 10. Differences (residuals) between the theoretical and estimated misorientations with different levels of coloured noise, which are shown at the lower-right-hand corner of each panel.

Table 3. Average SNR of the vertical-component seismograms and errors of synthetic data with different levels of noise.

Noise	0 per cent	10 per cent	20 per cent	30 per cent	40 per cent	50 per cent
SNR	4.2576×10^4	7.2713	4.0496	2.9897	2.4670	2.1559
MAD	7.3533×10^{-7}°	2.2591°	7.1635°	14.5500°	15.6403°	17.7580°

Table 4. Average SNR of the vertical-component seismograms recorded at the five OBSs in the Yap region.

Station	Y05	Y20	Y24	Y33	Y39
SNR	4.5197	9.4573	5.9785	5.9719	5.0641

After that, we conducted forward-modelling to obtain 359 synthetic data sets, each of which contains three-component synthetic waveforms for the models M1, M2 and M3 with the misorientation changing from 1° to 359° with an interval of 1°. Then these synthetic data sets are fitted as observed data following the above-mentioned procedure to obtain 359 estimated misorientations that are shown in Figs S4(a)–S4(c). The test results (Figs 4a–c and Figs S4a–S4c) indicate that our method works well and is quite effective.

When calculating RFs based on the field data, if a large Gaussian parameter is adopted, some artificial seismic phases may appear, which could lead to an improper interpretation. Hence, we tested our method for a smaller Gaussian parameter, and the direct *P* wave is fused with Pbs. Thirty-six radial RFs for the model M2 with a Gaussian parameter of 2.5 and different rotating angles are calculated with a misorientation of 0° (Fig. S2d), and then they are fitted as observed data (Fig. 4d). Similarly, the synthetic data sets with different misorientations from 1° to 359° are fitted, and the results are shown in Fig. S4(d). The test results (Figs 4d and S4d) suggest that our method is also effective for smaller Gaussian parameters.

4 EXPERIMENTS WITH LAND STATION DATA

Generally speaking, land seismic stations have higher data quality and more accurate azimuth than those of OBSs. If the misorientation of land stations estimated by our method is close to zero, it can be further inferred that the APRF method is effective. Hence, we applied this method to estimate the misorientation of 61 land seismic stations in Shandong Province, China (Zheng *et al.* 2010). Teleseismic events with magnitudes greater than 5.0 and epicentral distances ranging from 30° to 90° during January 2015 to December 2015 are selected from the United States Geological Survey (USGS) earthquake catalogue. To calculate RFs, a Gaussian parameter of 2.5 and 100 iterations are adopted for the ITER-deconvolution. As a result, a total of 2718 RFs are obtained. Our method is used to obtain 2718 misorientations of the 61 land seismic stations based on every RF without stacking, and the results show that 90 per cent of the estimated misorientations are within ±14° (Fig. S5).

Because of the randomness of a single RF, all RFs recorded at the same station are stacked to estimate the misorientation of each station. All the results fall in a range of ±8°, and 92 per cent of the stations are within a range of ±5° (Fig. 5a), which are consistent with the results (Fig. 5b) estimated by the tangential receiver-function method (Janiszewski & Abers 2015), further indicating that our method is quite effective.

5 OBS EXPERIMENT AND MISORIENTATION

The Yap Trench is located to the south of the Mariana Trench in the Western Pacific Ocean, where the Caroline Plate is subducting beneath the Philippine Sea Plate (Fig. 6). To study the seismic structure and tectonic evolution of the Yap subduction zone, we conducted a passive OBS array experiment with seven I-4C broad-band

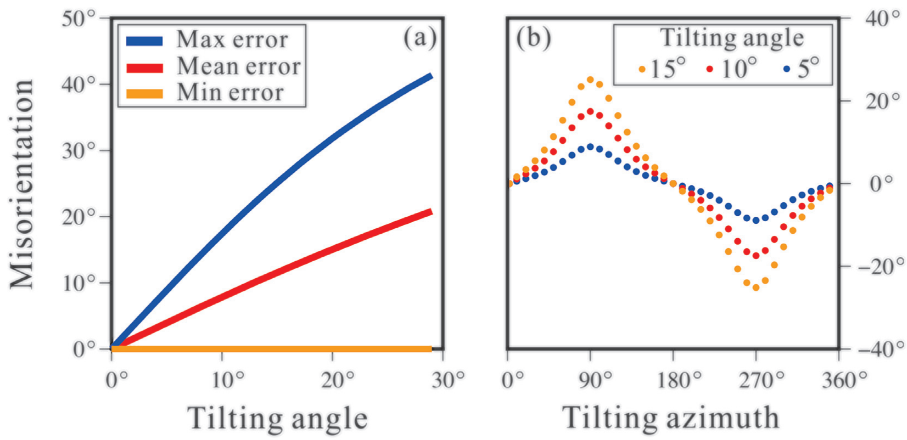

Figure 11. Errors of the estimated misorientations with different tilting angles (a) and azimuths (b). For the same tilting angle, the error reaches maximum when the tilting azimuths are 90° and 270°, whereas the error reaches minimum when the tilting azimuths are 0° and 180°, as shown in (b). The mean error in (a) denotes the average of absolute errors for all the tilting azimuths with the same tilting angle.

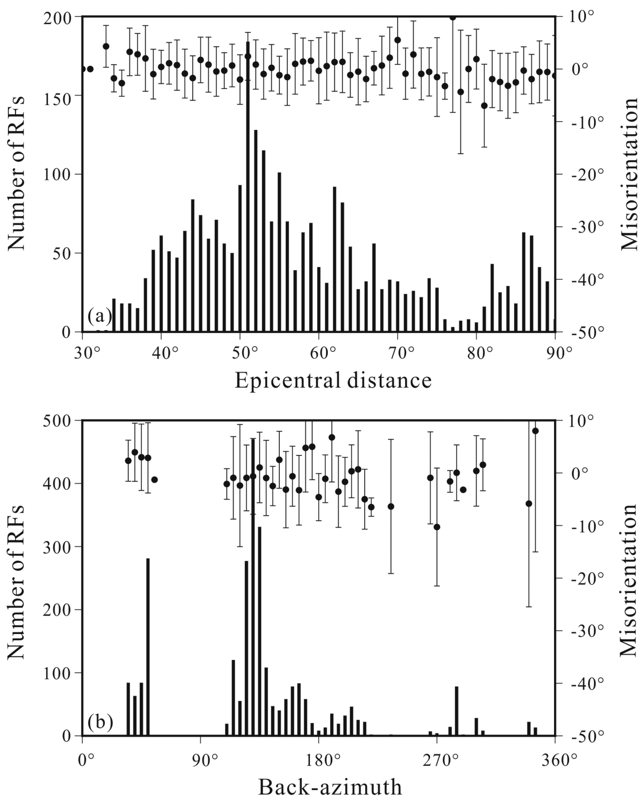

Figure 12. Number of RFs (thick bars) and the estimated misorientation (dots with thin error bars) versus the epicentral distance (a) and backazimuth (b). The intervals of the epicentral distance and backazimuth are 1° and 5°, respectively. The backazimuth coverage range (i.e. the number of RFs in one interval is >10) is 41.7 per cent.

OBSs in the Yap region using the research vessel *Kexue* (Science in Chinese) from the Institute of Oceanology, Chinese Academy of Sciences during April 2016 to May 2017 (Dong *et al.* 2018). These OBSs had 4 channels (including hydrophone) with a bandwidth of 0.0167–100 Hz. The sensitivity of the seismic sensors is greater than 200 V m^{-1} s^{-1}, and their sampling rate is 50 Hz. After 13 months deployment, 5 OBSs were successfully retrieved (Fig. 6), whose information is shown in Table S1.

To estimate misorientations of our OBS stations deployed in the Yap subduction zone, from the USGS earthquake catalogue we selected teleseismic events ($M \geq 6.0$) recorded at the OBSs with epicentral distances ranging from 25° to 90°. Generally speaking, when the low-velocity seafloor sediment exists, the direct *P*-wave polarization becomes nearly vertical, causing a low energy in the radial component, which may invalidate our method. To avoid this, seismograms used in this study (Fig. S6) are strictly selected to ensure that the direct *P*-wave amplitudes of the three-component original seismograms are big enough and have the same order of magnitude. A series of conventional pretreatments are conducted, including removing mean, linear trend, tapering and bandpass filtering (0.1–1 Hz). The Gaussian parameter is 10 and the iteration number is 100 for the ITER-deconvolution. As a result, 79 RFs from 30 teleseismic events with a SNR >4 are selected. Then these RFs at each OBS station are stacked with equal weighting to estimate misorientations. Fig. 7 and Table 2 show the fitting curves, fitting formulas and estimated misorientations for the five OBSs. In addition, Fig. 8 shows the RFs at the OBS stations Y20 and Y24 before and after the misorientation correction, which indicate that our method works very well.

If the estimated misorientation is accurate, the energy on the *R* and *T* components of seismograms after misorientation correction would be larger and smaller than that before misorientation correction, respectively. We calculated the mean energy of the *R* and *T* components in a window from 300 s before to 300 s after the direct *P*-wave arrival time. The results (Fig. S7) show that, for all five OBSs, the energy of the *R* component after the correction is higher than that before the correction, whereas the energy of the *T* component after the correction is lower than that before the correction, suggesting that the APRF method is effective and reliable.

Furthermore, if the sensor orientation is correct, the Love wave on the *T* component arrives earlier than the Rayleigh wave on the *Z* and *R* components, and the particle motion on the *Z*–*R* plane exhibits a counter-clockwise ellipse. To confirm this feature, we analysed the three-component seismograms and particle motion of an earthquake recorded at OBS Y39 before and after the misorientation correction (Fig. 9). The three-component waveforms after the misorientation correction show that the Love wave on the *T* component arrives earlier than the Rayleigh wave on the *Z* and *R* components (Fig. 9d), which is not visible on the three-component

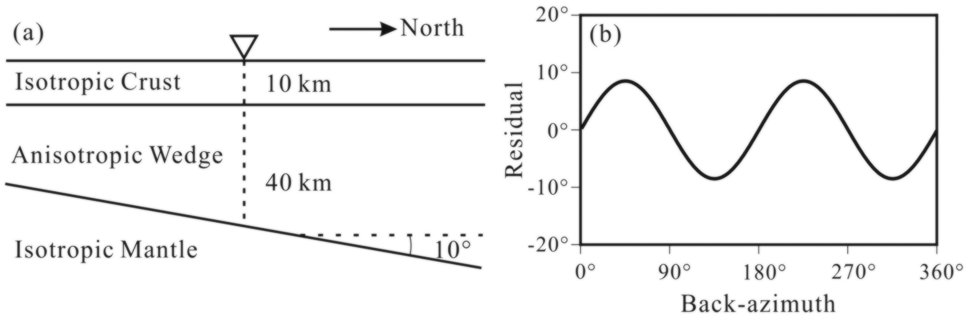

Figure 13. (a) A velocity model including an anisotropic and dipping layer. The inverted triangle denotes a seismic station. (b) Residuals between theoretical and estimated misorientations for different backazimuths.

Table 5. Physical parameters of the velocity model shown in Fig. 13. The fast-velocity direction, dipping direction and dipping angle of the wedge layer are 0°, 0° and 10°, respectively. The mantle is defined as a half-space.

Layer	Thickness (km)	ρ (g cm^{-3})	V_P (km s^{-1})	V_S (km s^{-1})	ΔP	ΔS
Crust	10	2.7	6.1	3.55	0	0
Wedge	40	3.5	7.9	4.4	10 per cent	10 per cent
Mantle	∞	4.4	8.1	4.55	0	0

waveforms before the misorientation correction (Fig. 9a). In addition, the particle motion on the *Z–R* plane after the misorientation correction shows a counterclockwise ellipse (Fig. 9e), quite different from that before the misorientation correction (Fig. 9b), and there are no such features on the *Z–T* plane before and after the misorientation correction (Figs 9c and f). These results indicate that misorientations of the five OBSs are precisely corrected.

6 DISCUSSION

6.1 Effect of noise

OBS waveforms usually have a high level of noise due to complex environment in the ocean, such as reverberations of water column and/or sedimentary layers (Audet 2016), ocean bottom currents and infragravity waves, which usually generate coloured noise (Crawford & Webb 2000; Bell *et al.* 2015). To investigate the influence of white and coloured noise on the APRF method, we added 10 per cent white and coloured noise at 0.1–1 Hz (Fig. S8) to the synthetic three-component (*R–T–Z*) waveforms generated for the model M1. Here the level of noise represents the ratio of the maximum amplitude of the noisy data to the maximum amplitude of the three-component waveform data. The fitting results with a misorientation of 20° are shown in Fig. S9, and errors of the fitting results are 0.53° and 2.18° for the white and coloured noise, respectively. We also tested different misorientations (from 0° to 360° with an interval of 1°) with white and coloured noise at the level of 10 per cent. The fitting results (Fig. S10) show that, although the mean absolute deviation (MAD) caused by the coloured noise is greater than that by the white noise, all the fitting results are reasonable.

To assess uncertainties of the estimated OBS misorientations with our method, we performed synthetic tests with different levels of coloured noise (10–50 per cent) using the procedure as mentioned above, that is three-component synthetic waveforms are generated for the model M1 with different levels of coloured noise. The fitting results, SNRs and MADs (Fig. 10 and Table 3) suggest that the APRF method is effective even with a high level of noise. The maximum uncertainty of the OBS misorientation is estimated to be about 7° by averaging the results of these tests, because the OBS SNRs are generally greater than 4.0 (Table 4).

6.2 Effect of sensor tilting

One reason for the difficulty of RF analysis of OBS data is failure of the OBS leveling system (Crawford & Webb 2000; Dahm *et al.* 2006; Bell *et al.* 2015; Tran *et al.* 2019). Similarly, the estimated OBS misorientation using our method depends on the tilting condition of each OBS, which includes two parameters: tilting angle and azimuth. A series of synthetic tests with the model M1 are conducted to evaluate the effects of sensor tilting on the sensor misorientation estimation (Fig. 11). In these tests, different tilting angles (0–29° with interval of 1°) and azimuths (0–360° with interval of 10°) are considered without sensor misorientation. As the tilting angle increases, the error of the estimated misorientation becomes larger (Fig. 11a). With the same tilting angle, the error of the estimated misorientation changes with the tilting azimuth and reaches its maximum and minimum when the tilting azimuth is the same as that of the transverse (i.e. ~90° and 270°) and radial components (i.e. ~0° and 180°), respectively (Fig. 11b). These results may be ascribed to the leakage of energy in the vertical component to the horizontal components, causing alternation and even polarity reversing of the direct *P* wave of RFs. Therefore, it is necessary to make the tilting correction before estimating the misorientation with our method.

For the OBSs deployed in the Yap subduction zone, there are gimbals inside, and the sensor tilting is adjusted every 4 hr. Therefore, we consider that these OBSs are not tilted, and their orientations are reliably estimated with the APRF method.

6.3 Effect of epicentral distance and backazimuth

The epicentral distance controls the ray parameter, which affects arrival times of converted and multiple phases of the receiver function (Fig. S11). However, our synthetic tests show that the change of epicentral distance does not affect the direct *P* wave of RF. Although the direct *P*-wave amplitude changes with the ray parameter, the amplitude for any other misorientation is not greater than that with the correct orientation. We performed two tests to investigate the influence of epicentral distance. In the first test, the RFs are weighted and stacked based on the epicentral distances of the teleseismic events. The test results (Fig. S12) are very similar to those obtained by the equal stacking (Fig. 5a). In the second test, the distribution of the estimated misorientations with different epicentral distances is obtained (Fig. 12a), most of which are around 0°. The two test results indicate that the misorientation estimated with our

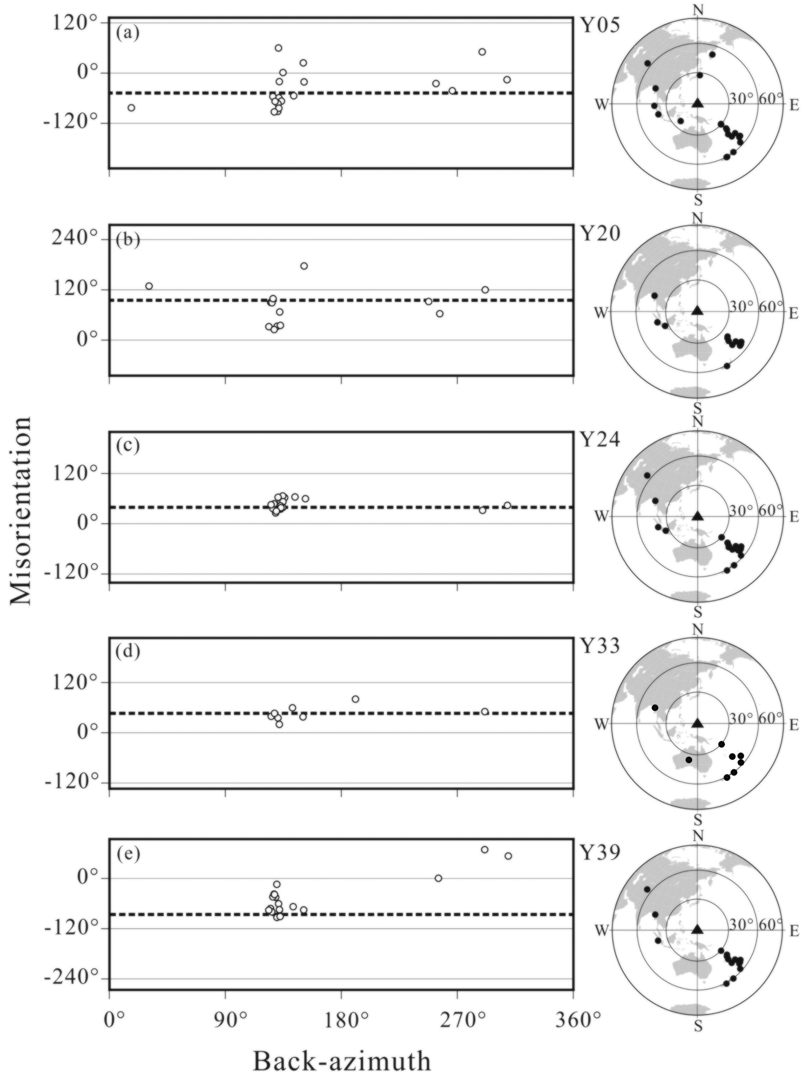

Figure 14. (a)–(e) Misorientations estimated from unstacked RFs (circles) and stacked RF (horizontal dashed lines) for five OBSs with different backazimuths. The maps on the right show the corresponding distribution of teleseismic events (dots) used to estimate the OBS misorientation.

method is not influenced by the epicentral distances of teleseismic events.

In the two synthetic tests, a homogeneous and isotropic layered velocity model is adopted. However, when an anisotropic and/or dipping layer exists, polarity reversals of some phases of RFs would occur in different backazimuths (Nagaya *et al.* 2008; Ford *et al.* 2016). To evaluate whether or not different backazimuths could cause deviations of the estimated misorientation with our method, we adopt a model including an anisotropic and dipping layer that has a fast-velocity direction of 0°, a dipping direction of 0° and a dipping angle of 10° (Fig. 13a and Table 5). Three-component synthetic waveforms are calculated using the reflectivity method (Frederiksen & Bostock 2000) for different backazimuths with a reference ray parameter of 0.07 s km^{-1} and a misorientation of 0°. Then we estimate the misorientation using our method for different backazimuths. The result shows that the residuals are less than 10° and characterized by a four-lobed curve with a 180° periodicity (Fig. 13b), which is consistent with the results of other synthetic tests (Wang *et al.* 2016). This test result indicates that the influence of the anisotropic and dipping layer on the misorientation estimation is relatively small, probably because *P*-wave propagation in the anisotropic media produces a quasi-*P* wave whose particle motion is not parallel to the propagation direction (Crampin *et al.* 1982).

In addition, we calculated misorientations of the land stations in Shandong Province and our OBSs for different backazimuths (Figs 12b and 14). The results show that some of the residuals may be affected by the anisotropic and dipping structure. Therefore, in areas with complicated underground structures, several different methods should be used to compare the obtained results so as to determine a more accurate misorientation.

6.4 Comparison with other methods

We also estimated the OBS misorientations using the *P*-wave particle motion methods, including the principal component analysis (PCA) and minimizing *T* energy methods (Niu & Li 2011; Wang *et al.* 2016), as well as the Rayleigh wave polarization method (Stachnik *et al.* 2012; Rueda & Mezcua 2015). The estimated results using the *P*-wave particle motion and the Rayleigh wave polarization methods are shown in Figs S13–S17 and Figs S18–S22, respectively, which are generally consistent with the results obtained with our APRF method (Table 6).

Table 6. OBS misorientations in the Yap subduction zone estimated with different methods. The Rayleigh wave polarization method is failed to calculate the misorientation of OBS Y24 (see Fig. S20).

Method/ station	*P*-wave particle motion		Rayleigh wave polarization	APRF
	Principal component analysis	Minimizing *T* energy		
Y05	− 37.60° ± 19.48°	− 37.20° ± 8.30°	− 33.18° ± 11.75°	− 47.43° ± 6.45°
Y20	107.35° ± 16.15°	110.50° ± 6.40°	120.53° ± 18.99°	95.07° ± 2.26°
Y24	42.59° ± 13.89°	43.00° ± 6.50°	–	39.24° ± 4.23°
Y33	54.08° ± 17.92°	53.00° ± 6.70°	40.82° ± 15.59°	46.46° ± 4.24°
Y39	− 85.34° ± 8.25°	− 86.20° ± 4.80°	− 92.84° ± 8.14°	− 85.88° ± 5.62°

The *P*-wave particle motion method is very popular for investigating the *S*-wave velocity structure (Svenningsen & Jacobsen 2007; Hannemann *et al.* 2016; Knapmeyer-Endrun *et al.* 2018), and it can also estimate the sensor misorientation (Niu & Li 2011; Wang *et al.* 2016). However, the result error by our method is smaller than that by the PCA method, ascribed to the deconvolution used in our method to significantly reduce the effect of the ambient noise near the seafloor, instead of the original waveforms used for the *P*-wave particle motion method. In addition, the *P*-wave particle motion method estimates two optimal misorientations, because the period is π. Although a precise solution could be determined by using cross-correlation between the vertical and horizontal components, it is a little difficult to figure out which one is more appropriate because of noise, frequency band and the selection of time window of waveforms. A wrongly estimated misorientation would cause serious problems to other seismological studies.

Furthermore, the uncertainties of the estimated misorientations using the Rayleigh wave polarization method are slightly larger (Table 6). This is because the dominant period band of the surface waves is 18–22 s (Stachnik *et al.* 2012), coinciding with the period of the ambient noise near the seafloor, such as infragravity waves (Crawford & Webb 2000), microseisms induced by surface water waves (Friedrich *et al.* 1998) and bottom currents (Bell *et al.* 2015). In addition, the selection of the time window of Rayleigh wave is difficult because of the high-level noise. For example, the uncertainties of estimation using the Rayleigh wave polarization method are up to ±80° at stations in the Cascadia region (Janiszewski & Abers 2015). Therefore, it would be better to remove the noise before using the Rayleigh wave polarization method, which is usually quite difficult.

7 CONCLUSIONS

In this study, a new method is developed to correct OBS misorientation by fitting the amplitude of direct *P* wave of teleseismic radial receiver functions. The effectiveness of this method is firstly verified by using synthetic data and observed data at land seismic stations in Shandong Province, China. Then the method is applied to estimate orientations of five OBSs deployed in the Yap subduction zone. By using a higher Gaussian parameter, the interference of sedimentary layers on the direct *P* wave can be avoided. The influence of white and coloured noise level on the sensor misorientation is evaluated, which indicates that our method is not affected significantly by even high-level noise. Our analysis shows that the sensor tilting has a large influence on the misorientation, and so it is necessary to make tilting correction before estimating the sensor orientation using our method. Anisotropy or dipping layers have small periodic influence on our method with backazimuth. Compared with other methods, our method is more effective, and our estimates of misorientation are reliable for the five OBS sensors deployed in the Yap subduction zone.

ACKNOWLEDGEMENTS

We are grateful to the scientists and crews of the research R/V *Kexue*, who provided technical assistance for deploying and retrieving the OBSs. OBS data were acquired by the Chinese Academy of Sciences' Strategic Priority Research Program. Waveform data recorded at land seismic stations in Shandong Province for this study are provided by the Data Management Centre of the China National Seismic Network at Institute of Geophysics, China Earthquake Administration (SEISDMC, doi:10.7914/SN/CB). We thank Drs Zhiwei Li, Rong Huang, You Tian, Xin Wang, Hongxiang Zhu and Yanan Liu for helpful discussions. This work was financially supported by the National Natural Science Foundation of China (Nos. 41876043, 91958211) to H. Zheng and J. Fan, the Key Deployment Project of Center for Ocean Mega-Research of Science, Chinese Academy of Sciences (No. COMS2019Q10) to D. Dong, C. Li, G. Zhang and X. Wang, as well as a research grant from Japan Society for the Promotion of Science (19H01996) to D. Zhao. In the data analyses, we used the Generic Mapping Tools (GMT, Wessel *et al.* 2013), the USGS earthquake catalogue (https://earthquake.usgs.gov/) and the Incorporated Research Institutions for Seismology (IRIS) for SAC101.6a and Taup. The receiver-function calculation was made using the computer programs in seismology (http://www.eas.slu.edu/eqc/eqccps.html). Prof. Martin Schimmel (the Editor) and three anonymous referees provided thoughtful review comments and suggestions that have greatly improved this paper.

REFERENCES

Ammon, C.J., Ranndall, G.E. & Zandt, G., 1990. On the nonuniqueness of receiver function inversion, *J. geophys. Res.,* **95**(B10), 15 303–15 318.

Audet, P., 2016. Receiver functions using OBS data: promises and limitations from numerical modeling and examples from the Cascadia Initiative, *Geophys. J. Int.,* **205,** 1740–1755.

Baker, G.E. & Stevens, J.L., 2004. Backazimuth estimation reliability using surface wave polarization, *Geophys. Res. Lett.,* **31,** L09611, doi:10.1029/2004GL019510.

Bell, S.W., Forsyth, D.W. & Ruan, Y., 2015. Removing noise from the vertical component records of ocean-bottom seismometers: results from year one of the Cascadia Initiative, *Bull. seism. Soc. Am.,* **105**(1), 300–313.

Crampin, S., Stephen, R.A. & McGonigle, R., 1982. The polarization of P-waves in anisotropic media, *Geophys. J. R. astr. Soc.,* **68,** 477–485.

Crawford, W.C. & Webb, S.C., 2000. Removing tilt noise from low frequency (<0.1 Hz) seafloor vertical seismic data, *Bull. seism. Soc. Am.,* **90**(4), 952–963.

Dahm, T., Tilmann, F. & Morgan, J.P., 2006. Seismic broadband ocean-bottom data and noise observed with free-fall stations: experiences from long-term deployments in the North Atlantic and the Tyrrhenian Sea, *Bull. seism. Soc. Am.,* **96**(2), 647–664.

Dong, D., Zhang, Z., Bai, Y., Fan, J. & Zhang, G., 2018. Topographic and sedimentary features in the Yap subduction zone and their implications for the Caroline Ridge subduction, *Tectonophysics,* **722,** 410–421.

Ford, H.A., Long, M.D. & Wirth, E.A., 2016. Midlithospheric discontinuities and complex anisotropic layering in the mantle lithosphere beneath the Wyoming and Superior Provinces, *J. geophys. Res.,* **121**(9), 6675–6697.

Frederiksen, A.W. & Bostock, M.G., 2000. Modelling teleseismic waves in dipping anisotropic structures, *Geophys. J. Int.,* **141,** 401–412.

Friedrich, A., Krüger, F. & Klinge, K., 1998. Ocean-generated microseismic noise located with the Gräfenberg array, *J. Seismol.,* **2,** 47–64.

Hannemann, K., Krüger, F., Dahm, T. & Lange, D., 2016. Oceanic lithospheric S-wave velocities from the analysis of P-wave polarization at the ocean floor, *Geophys. J. Int.,* **207,** 1796–1817.

Herrmann, R.B. & Mandal, B., 1986. A study of wavenumber integration techiques, *Earthq. Notes,* **57**(2), 33–40.

Janiszewski, H.A. & Abers, G.A., 2015. Imaging the plate interface in the Cascadia seismogenic zone: new constraints from offshore receiver functions, *Seismol. Res. Lett.,* **86**(5), 1261–1269.

Julià, J., Ammon, C.J., Herrmann, R.B. & Correig, A.M., 2000. Joint inversion of receiver function and surface-wave dispersion observations, *Geophys. J. Int.,* **143**(1), 99–112.

Kawakatsu, H. & Abe, Y., 2016. Comment on "Nature of the seismic lithosphere- asthenosphere boundary within normal oceanic mantle from high-resolution receiver functions" by Olugboji et al, *Geochem. Geophys. Geosyst.,* **17,** 3488–3492.

Kennett, B.L.N. & Engdahl, E.R., 1991. Traveltimes for global earthquake location and phase identification, *Geophys. J. Int.,* **105,** 429–465.

Kikuchi, M. & Kanamori, H., 1982. Inversion of complex body waves, *Bull. seism. Soc. Am.,* **72**(2), 491–506.

Knapmeyer-Endrun, B., Ceylan, S. & van Driel, M., 2018. Crustal S-wave velocity from apparent incidence angles: a case study in preparaton for insight, *Space Sci. Rev.,* **214**(83), 123.

Laske, G., Masters, G. & Zurn, W., 1994. Frequency-dependent polarization measurements of long-period surface waves and their implications for global phase-velocity maps, *Phys. Earth planet. Inter.,* **84,** 111–137.

Laske, G., 1995. Global observation of off-great-circle propagation of long-period surface-waves, *Geophys. J. Int.,* **123,** 245–259.

Langston, C.A., 1979. Structure under Mount Ranier, Washington, inferred from teleseismic body waves, *J. geophys. Res.,* **84,** 4749–4762.

Ligorria, J.P. & Ammon, C.J., 1999. Iterative deconvolution and receiver-function estimation, *Bull. seism. Soc. Am.,* **89**(5), 1395–1400.

Lim, H., Kim, Y., Song, T.A. & Shen, X., 2018. Measurement of seismometer orientation using the tangential P-wave receiver function based on harmonic decomposition, *Geophys. J. Int.,* **212,** 1747–1765.

Long, M.D., Gao, H., Klaus, A., Wagner, L.S., Fouch, M.J., James, D.E. & Humphreys, E., 2009. Shear wave splitting and the pattern of mantle flow beneath eastern Oregon, *Earth planet. Sci. Lett.,* **288,** 359–369.

Nagaya, M., Oda, H., Akazawa, H. & Ishise, M., 2008. Receiver functions of seismic waves in layered anisotropic media: application to the estimate of seismic anisotropy, *Bull. seism. Soc. Am.,* **98**(6), 2990–3006.

Niu, F. & Li, J., 2011. Component azimuths of the CEArray stations estimated from P-wave particle motion, *Earthq. Sci.,* **24,** 3–13.

Owens, T.J., Zandt, G. & Taylor, S.R., 1984. Seismic evidence for an ancient rift beneath the Cumberland Plateau, Tennessee: a detailed analysis of broadband teleseismic P waveforms, *J. geophys. Res.,* **89,** 7783–7795.

Pimm, A.C., Garrison, R.E. & Boyce, R.E., 1971. Sedimentology synthesis: lithology, chemistry and physical properties of sediments in the northwestern Pacific Ocean, *DSDP website,* 1131–1152, doi:10.2973/dsdp.proc.6.138.1971.

Ringler, A.T., Hutt, C.R., Persefield, K. & Gee, L.S., 2013. Seismic station installation orientation errors at ANSS and IRIS/USGS stations, *Seismol. Res. Lett.,* **84,** 926–931.

Rueda, J. & Mezcua, J., 2015. Orientation analysis of the Spanish broadband national network using rayleigh-wave polarization, *Seismol. Res. Lett.,* **86**(3), 929–940.

Sheehan, A.F., Abers, G.A., Jones, C.H. & Lerner-Lam, A.L., 1995. Crustal thickness variations across the Colourado Rocky Mountains from teleseismic receiver functions, *J. geophys. Res.,* **10**(B10), 20391–20404.

Stachnik, J.C., Sheehan, A.F., Zietlow, D.W., Yang, Z., Collins, J. & Ferris, A., 2012. Determination of New Zealand ocean bottom seismometer orientation via Rayleigh-wave polarization, *Seismol. Res. Lett.,* **83,** 704–713.

Svenningsen, L. & Jacobsen, B.H., 2007. Absolute S-velocity estimation from receiver functions, *Geophys. J. Int.,* **170,** 1089–1094.

Tran, D.H., Yang, T., Le, B.M. & Yu, Y., 2019. Effects of failure of the ocean-bottom seismograph leveling system on receiver function analysis, *Seismol. Res. Lett.,* **90** (3), 1191–1199.

Vinnik, L.P., 1977. Detection of waves converted from P to SV in the mantle, *Phys. Earth planet. Inter.,* **15,** 39–45.

Wang, X., Chen, Q., Li, J. & Wei, S., 2016. Seismic sensor misorientation measurement using P-wave particle motion: an application to the NECsaids array, *Seismol. Res. Lett.,* **87**(4), 901–911.

Wessel, P., Smith, W.H., Scharroo, R., Luis, J. & Wobbe, F., 2013. Generic mapping tools: improved version released, *EOS, Trans. Am. geophys. Un.,* **94**(45), 409–410.

Zahradnik, J. & Custodio, S., 2012. Moment tensor resolvability: application to southwest Iberia, *Bull. seism. Soc. Am.,* **102,** 1235–1254.

Zha, Y., Webb, S.C. & Menke, W., 2013. Determining the orientations of ocean bottom seismometers using ambient noise correlation, *Geophys. Res. Lett.,* **40,** 3585–3590.

Zhang, Z., Dong, D., Sun, W., Wu, S., Bai, Y., Wang, X. & Fan, J., 2019. Subduction erosion, crustal structure, and an evolutionary model of the northern Yap subduction zone: new observations from the latest geophysical survey, *Geochem. Geophys. Geosyst.,* **20,** 166–182.

Zheng, X., Yao, Z., Liang, J. & Zheng, J., 2010. The role played and opportunities provided by IGP DMC of China National Seismic Network in Wenchuan earthquake disaster relief and researches, *Bull. seism. Soc. Am.,* **100**(5B), 2866–2872.

Zhu, L. & Kanamori, H., 2000. Moho depth variation in southern California from teleseismic receiver functions, *J. geophys. Res.,* **105,** 2969–2980.

SUPPORTING INFORMATION

Supplementary data are available at *GJI* online.

Figure S1. RFs calculated with different values of thickness (a) and *S*-wave velocity (b) of a sedimentary layer. In panels (a) and (b), the other parameters are from the model M2. The Gaussian parameter is 2.5. (c) Schematic ray paths of different seismic phases in a receiver function.

Figure S2. Teleseismic receiver functions for rotating angles from 0° to 360° with an interval of 10° for the models M1 (a), M2 (b), M3 (c) and M2 (d) with different Gaussian parameters (G).

Figure S3. Variations of the amplitude with different rotating angles (dots) with fixed misorientations of 135° (a) and 225° (b). The thick grey lines are the fitting cosine curves. The fitting formulas are (a) : $\mathrm{A}_{rf}\ (\mathrm{x}) =\ 0.7802{*}\cos(\mathrm{x} + 135 + 5.125 \times 10^{-8})$ and (b) : $A_{rf}\ (x) =\ 0.7802{*}\cos(\mathrm{x} + 225 + 5.137 \times 10^{-8})$.

Figure S4. Residuals between theoretical and estimated misorientations.

Figure S5. Distribution of misorientations of 61 land seismic stations estimated from 2718 unstacked receiver functions of teleseismic events as shown in the inset map. The triangle in the map denotes the center of the land seismic network in Shandong Province, China. The dashed lines denote the cutoff misorientations at ±14. The interval of misorientation is 1°.

Figure S6. Three-component seismograms of an earthquake (M_{w} 6.8) recorded at OBS Y20. Its epicentral distance and focal depth are 36.64° and 169 km, respectively.

Figure S7. Ratios of energy after the misorientation correction to that before the correction in the radial (dots) and transverse (triangles) components at five OBSs deployed in the Yap region.
Figure S8. Time-series (a, c) and amplitude spectra (b, d) of the white (a, b) and coloured (c, d) noise at a level of 10 per cent.
Figure S9. Variations of the amplitude with different rotating angles (dots) with 10 per cent white (a) and coloured (b) noise for a misorientation of 20°. The thick grey lines are the fitting cosine curves. The fitting formulas are (a) : $A_{rf}\ (x) =\ 2.839{*}\cos(x + 19.47)$ and (b) : $A_{rf}\ (x) =\ 1.694{*}\cos(x + 22.18)$.
Figure S10. Residuals between theoretical and estimated misorientations with 10 per cent white (a) and coloured (b) noise.
Figure S11. RFs generated for the model M1 with different ray parameters. The epicentral distances of the RFs in the blue box are from 25° to 90°.
Figure S12. Histogram of the station misorientations determined by weighted stacking on the basis of epicentral distances. The misorientation interval is 1°.
Figure S13. Misorientation of OBS Y05 [red triangular in (a)] estimated using the *P*-wave particle motion method. Θ_{minT}, Θ_{PCA} and Θ_{APRF} denote the results obtained using the minimum *T* energy method, the principal component analysis method and our new method (APRF), respectively. (a) Distribution of the earthquakes (blue dots) used. (b) The red line denotes the summed energy of the *T* components for a suite of events, whereas the blue dot represents the estimated misorientation that is determined by minimizing the summed energy of the *T* component. (c) The red triangles represent the estimated misorientations using the single-earthquake PCA method. The green squares are the cross-correlation coefficients between the vertical and radial components [$cc(Z/R)$]. The blue solid line and grey area denote the misorientation and its error range estimated by minimizing the *T* energy measurement.
Figure S14. The same as Fig. S13 but for OBS Y20.
Figure S15. The same as Fig. S13 but for OBS Y24.
Figure S16. The same as Fig. S13 but for OBS Y33.
Figure S17. The same as Fig. S13 but for OBS Y39.
Figure S18. Misorientation estimation for OBS Y05 in a frequency band 0.02–0.04 Hz using the Rayleigh wave polarization method. Θ_{RWP} and Θ_{APRF} denote the results obtained using the Rayleigh wave polarization method and our new method (APRF), respectively. (a) Distribution of teleseismic events (dots) used for the estimation. (b) Polar histogram representation of the orientations. (c) Distribution of the orientations indicated by a single earthquake (dots) and the correlation coefficients (C_{zr}), which equals the ratio of S_{zr} to S_{zz} that serve as indexes for the waveform quality. S_{zr} means zero-lag cross correlation between the *Z* component and the Hilbert-transformed *R*-component. S_{zz} means autocorrelation of the *Z* component. The vertical solid line shows the minimum correlation coefficient (0.5) cutoff value. The horizontal dashed line indicates the orientation of the weighted average using the dots on the right-hand side of the vertical solid line. The angle between the values indicated by the horizontal dashed line to the north indicated by 360° (c) is the misorientation.
Figure S19. The same as Fig. S18 but for OBS Y20.
Figure S20. The same as Fig. S18 but for OBS Y24. The results obtained from different earthquakes are very scattered, and so we are unable to estimate the sensor orientation.
Figure S21. The same as Fig. S18 but for OBS Y33.
Figure S22. The same as Fig. S18 but for OBS Y39.
Table S1. Basic information of the OBS stations deployed in the Yap region.